Automatic Symmetry Detection From Brain MRI Based on a 2-Channel Convolutional Neural Network

Huisi Wu, Xiujuan Chen, Ping Li, *Member, IEEE*, and Zhenkun Wen

***Abstract*—Symmetry detection is a method to extract the ideal mid-sagittal plane (MSP) from brain magnetic resonance (MR) images, which can significantly improve the diagnostic accuracy of brain diseases. In this article, we propose an automatic symmetry detection method for brain MR images in 2-D slices based on a 2-channel convolutional neural network (CNN). Different from the existing detection methods that mainly rely on the local image features (gradient, edge, etc.) to determine the MSP, we use a CNN-based model to implement the brain symmetry detection, which does not require any local feature detections and feature matchings. By training to learn a wide variety of benchmarks in the brain images, we can further use a 2-channel CNN to evaluate the similarity between the pairs of brain patches, which are randomly extracted from the whole brain slice based on a Poisson sampling. Finally, a scoring and ranking scheme is used to identify the optimal symmetry axis for each input brain MR slice. Our method was evaluated in 2166 artificial synthesized brain images and 3064 collected *in vivo* MR images, which included both healthy and pathological cases. The experimental results display that our method achieves excellent performance for symmetry detection. Comparisons with the state-of-the-art methods also demonstrate the effectiveness and advantages for our approach in achieving higher accuracy than the previous competitors.**

***Index Terms*—2-channel convolutional neural network (CNN), brain MRI, deep learning, mid-sagittal plane (MSP) detection, symmetry detection.**

I. Introduction

With the rapid development of medical image analysis, we can extract useful high-level information from a large amount of existing medical raw data to assist diagnoses. As many organs of our human body are nearly symmetrical, symmetry is one of the useful high-level features. Actually, if an organ is found to be approximately asymmetrical, it is likely to be caused by the pathological changes [1]. A human brain has two apparently similar hemispheres, where the brain is divided into two parts separated by the fissure interhemispheric [2]. Usually, we name the middle plane of the fissure interhemispheric as the mid-sagittal plane (MSP), because it is a perpendicular plane to divide the brain into left and right parts under a virtual geometric plane. A typical example of MSP detection in brain images is shown in Fig. 1. The anatomical tissues of the human brain reach maximum symmetry on both sides of MSP. Currently, it is proved that the approximate symmetry of the brain changes with the lesion, possibly resulting in changes in brain structure or tissue texture, such as mental illness [3], [4]; brain injury [5], [6]; brain tumors [7]; and neurodegenerative changes [8].

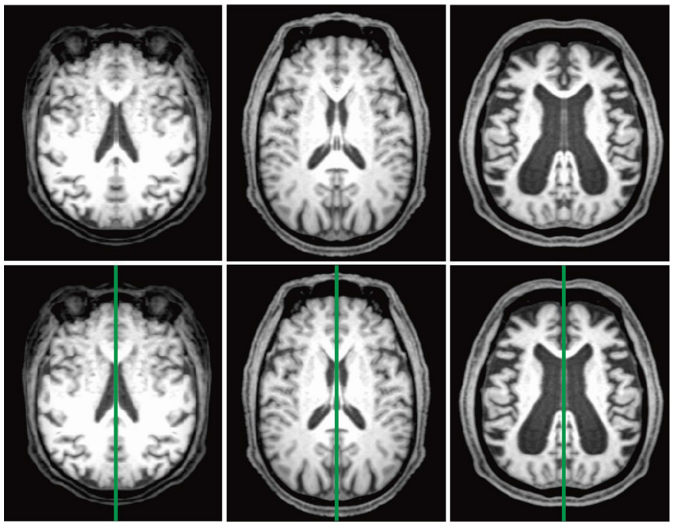

Fig. 1. Symmetry detection of brain MRI. MSP is extracted in each brain image.

For the requirement of the practical applications, symmetry detection and MSP extraction of brain image have a significant impact in image registration, brain segmentation, pathological detection, and medical image classification. For instance, the MSP detection is often the preprocessing step in spatial normalization or anatomical standardization of brain images [9] using automatic extraction of pathological brain slices and tumor segmentation. Therefore, symmetry analysis of the brain image is regarded as a promising and necessary technique.

Manuscript received June 26, 2019; revised September 22, 2019; accepted November 6, 2019. Date of publication November 28, 2019; date of current version September 8, 2021. This work was supported in part by the National Natural Science Foundation of China under Grant 61973221, in part by the Natural Science Foundation of Guangdong Province of China under Grant 2018A030313381 and Grant 2019A1515011165, and in part by the Hong Kong Polytechnic University under Grant P0030419 and Grant P0030929. This article was recommended by Associate Editor C.-T. Lin. *(Corresponding author: Huisi Wu.)*

H. Wu, X. Chen, and Z. Wen are with the College of Computer Science and Software Engineering, Shenzhen University, Shenzhen 518000, China (e-mail: hswu@szu.edu.cn).

P. Li is with the Department of Computing, Hong Kong Polytechnic University, Hong Kong (e-mail: p.li@polyu.edu.hk).

Color versions of one or more figures in this article are available at https://doi.org/10.1109/TCYB.2019.2952937.

Digital Object Identifier 10.1109/TCYB.2019.2952937

However, symmetry detection from brain magnetic resonance (MR) images is still challenging and remains an important task after decades of research. Currently, there are two main categories of the MSP detection methods. The first one is based on symmetry to locate MSP, and the second category is based on image recognition. But most of the existing methods for brain symmetry detection mainly rely on the local image feature detection and feature matching [10]. As the complexity of the feature selection for brain structures and various noise artifacts in brain MR images, the accuracy of the feature-based methods still cannot reach the requirement of the real applications. Recently, the deep-learning technique provides an automatic framework for applications for computer vision [11]–[13], which also opens a new space for medical image analysis.

In this article, we propose a novel symmetry detection method for brain MR images based on the convolutional neural network (CNN) model. Unlike the conventional feature-based brain symmetry detection methods, our approach is a learning-based method that does not require any feature detection and matching operations. Specifically, Poisson sampling is used to extract several pairs of brain image patches, which could have various resolutions. We then use a 2-channel CNN to compare one brain patch with its corresponding brain patch. Finally, a scoring and ranking algorithm is proposed to obtain the optimal symmetry axis for the brain MR slice. To the best of our knowledge, our method is the first attempt to employ this deep learning framework to extract the fissure line by learning a symmetry representation (fissure line) for the human brain. The stable and real-time performance has been demonstrated by the effectiveness of our method in achieving a high accuracy of symmetry detection. We evaluated our method using both artificially synthesized brain images and the collection *in vivo* MR images. The experimental results demonstrated the effectiveness and advantages of our purpose in achieving higher accuracy than the existing feature-based brain symmetry detection methods.

II. Related Work

Symmetry detection for brain MR images remains a hot topic in medical image analysis. As MSP plays an essential role in the brain MR image analysis, many brain symmetry detection methods have been proposed in the past decades [14]–[16]. Currently, the existing MSP detection methods can be mainly divided into two categories [17]. One of them is to extract the MSP by maximizing the symmetry score according to the symmetry. Instead, another one is to extract MSP based on the pattern recognition method.

The first kind of MSP extraction method assumes global bilateral symmetry to maximize similarity measurements between original brain scans and its reflective versions. Zhang and Hu [18] first described an efficient PCA outline to represent MSP images. Liu *et al.* [19] then detected the most matching symmetric plane by deploying the shape-based criteria. Ray *et al.* [20] also described a real-time algorithm to cut brain tumor using the symmetry of the brain MR Images based on the partial symmetry of the brain. Furthermore, Hu and Nowinski [21] located fissure line segments by minimizing the local symmetry index. Cornelius and Loy [22] proposed a feature detector and descriptor independently to detect planar rotational symmetry under affine projection. More recently, Wu *et al.* [23] extracted the MSP by maximizing global symmetry which was fitted by detecting the symmetry constraint feature points. Liao *et al.* [24] detected symmetry by means of asymmetric quantification. These symmetry detection methods can be applied to other image processing. But above symmetry-based algorithms rely heavily on the image features, which also often require complex image preprocessing and thus with unsatisfied precision.

On the other hand, several MSP extraction methods are based on pattern recognition. Xiao *et al.* [25] first proposed a method to measure MSP by identifying a thin layer of the septum pellucidum between the frontal horn and the lateral ventricle in a given CT study. Ferrari *et al.* [26] also proposed a slice thickness measurement method by iteratively detecting the MSP in MR image by the weighted least-squares fitting algorithm. Liu and Dawant [27] used the regression forests method to locate the plane automatically. However, most of these kinds of methods are limited by the training data which are used to build the models. Generally speaking, the pattern recognition-based methods are usually more robust than the first kind of methods, but they still cannot reach the expected accuracy due to the interference of local deformation, image noises, and outliers.

In recent years, deep learning is widely used as a filter library for feature extraction [28] and expression recognition [29], target motion detection [30], [31], medical services [32], etc. Especially, the CNNs have been widely used in the biomedical field, including segmentation [33]–[35], brain extraction [36], segmenting human left ventricle [37], reflection symmetry detection, etc. Typically, Kamnitsas *et al.* [38] used a multiscale 3-D CNN to segment brain injury. Shakeri *et al.* [39] used F-CNN to segment subcortical structures. Based on the deep-learning neural network, the hidden image features can be obtained. Without any specific feature detection and selection, we can implement many medical image analysis applications with very high accuracy. More important, compared with the traditional feature-based methods, it is proved in many practical applications that CNNs have a better potential prospect in computer graphics, computer vision, and medical image analysis domains.

In this article, we propose an automatic symmetry detection method for brain MR images based on a 2-channel CNN. Based on our defined 2-channel CNN, we can measure the variations of the appearance for both color and space domains in the brain images, without any specific image feature detection or selection. We also can learn a general patch similarity function directly from the original brain MR image, which is encoded in the form of a 2-channel CNN model. Our method automatically detects MSP based on the global symmetry of the brain image and the similarity of a brain image patch in the 2-channel network. The experimental results and comparison with state of the art demonstrated the effectiveness of the proposed method.

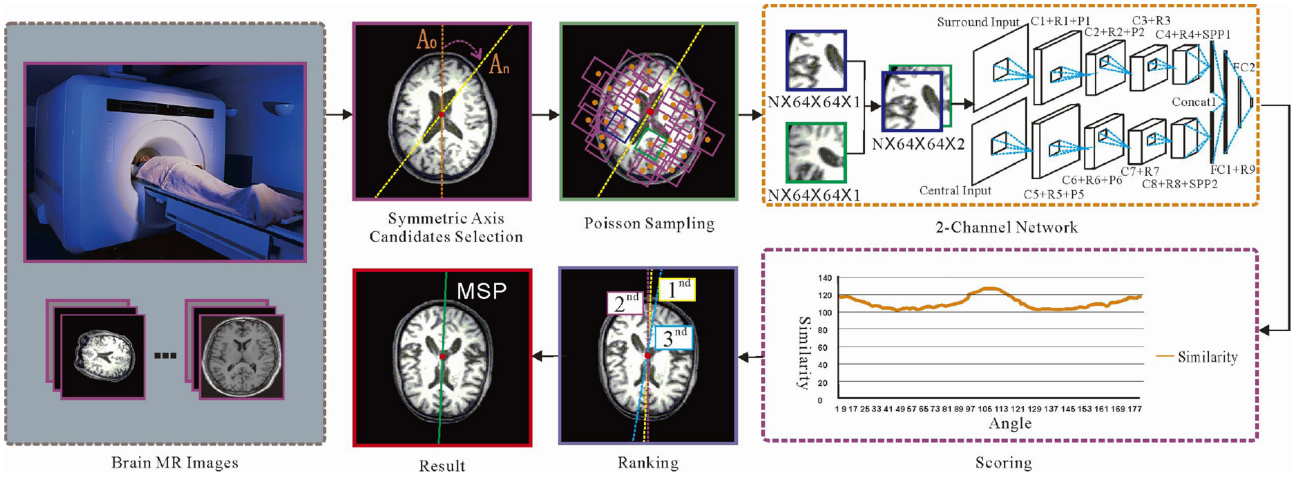

Fig. 2. Framework of our system.

III. Method

The framework of our proposed method is shown in Fig. 2. Given an MR brain image, we first obtain the image centroid from the external contour of the brain image and take the line passing through the centroid and perpendicular to the x-axis as the initial symmetry axis candidate. Then, a Poisson sampling algorithm is used to fetch a number of brain patches in the two sides of the symmetry axis. All sampled brain patches obtained in pairs are further put into our 2-channel CNN model to learn the similarity function. The sampling and the learning processes are repeated by rotating the initial candidate axis with a small step from 0° to 180° counterclockwise. Finally, we obtain the optimal symmetry axis according to the final scoring and ranking scheme.

A. Symmetry Axis Candidates Selection

Given a brain MR image (256×256), we first need to determine the initial position and the angle of the symmetry axis candidates. Obviously, the initial position of the symmetry axis is the first key step to implement our brain symmetry detection. In our experiment, we found that an excellent choice for symmetry axis initialization should pass through the center of mass for the brain, as shown in Fig. 3. To determine the centroid of the brain image C_0, we first employ an end-to-end HED network [40] to extract the external contour of the brain in the MR image. HED network was modified based on the VGG network, which has designed five lateral output layers. To improve the accuracy of edge detection, two pooling layers and all full connection layers of the VGG network were removed. In the meantime, we can also improve the significant edge abstraction with high accuracy and sensitivity for the texture edge on the brain images, as shown in Fig. 3(b).

After the brain contour extraction, we can further determine the initialization position for the symmetry axis by calculating the center of mass. As shown in Fig. 3(c), we can roughly capture the external contour for the brain based on the result of the HED network in Fig. 3(b). Meanwhile, we also collect the coordinate set of the contours. Let the coordinate of each pixel be (x_i, y_i). Then, we can easily obtain the coordinate of

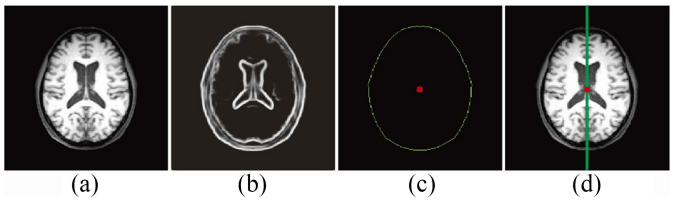

Fig. 3. Symmetry axis candidate selection. (a) Input. (b) Brain contours extracted with the HED network. (c) External brain contour and the brain centroid. (d) Initial symmetry axis candidate.

the brain centroid $C_0 = (x_c, y_c)$ via the following formulas:

$$x_c = \frac{1}{n}\sum_{i=1}^{n} x_i \tag{1}$$

$$y_c = \frac{1}{n}\sum_{i=1}^{n} y_i \tag{2}$$

where x_c and y_c represent the coordinate values of the x-axis and y-axis of the centroid, respectively. n is the number of pixels on the brain contours. So far, we can determine the initial position for the symmetry axis candidate by drawing a line passing through the C_0. As more than one line is passing through the C_0 in theory, in our experiment, we select the line perpendicular to the x-axis one as the initial symmetry axis candidate, as shown in Fig. 3(d).

B. Symmetric Patches Extraction

Based on the initial symmetry axis A_i, we can evaluate the symmetric relationship of the image content between the left and right parts besides the axis. One may directly compare the two subimages as a whole to implement global symmetry detection. However, this can easily obtain a wrong MSP due to the interruption of local deformation, tumor, and imaging noise. In our experiment, we assess the symmetric relationship of the two parts besides the axis based on a number of pairs of local brain patches. As shown in Fig. 4, we can randomly pick a pair of patches p_i and q_i from the left and right hemispheres beside the initial symmetry axis. Note that p_i and q_i have

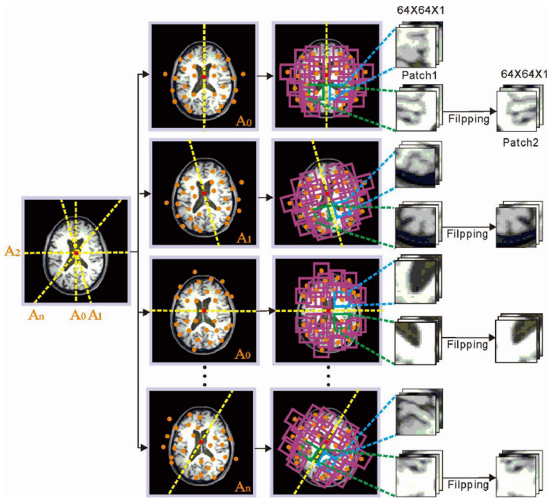

Fig. 4. Symmetry patches extraction based on the Poisson sampling.

a symmetric relationship according to the symmetry axis A_i. Then, we can evaluate the symmetric relationship between p_i and q_i by matching the two image patches.

As we assume the symmetry axis is a line passing through the centroid of the brain, we can generate a set of symmetry axis candidates by rotating the initial symmetry axis with a small step from 0° to 180° counterclockwise, as shown in Fig. 4. To chose the best axis from all symmetry axis candidates, we need to pick a number of pairs of symmetric patches to evaluate each axis candidate. For a simple implementation, one may suggest picking the local symmetric patches via a repeated randomly selection. Obviously, purely repeating the random selection for the local symmetric patches may occur in a nonuniform selection. More important, we cannot guarantee that all regions in the left and right hemispheres would be definitely picked after several times of random selection, because the nature of the randomizing can ultimately ignore some local brain regions. So we employ a Poisson disk sampling [41] in our local symmetric patches selection. Because Poisson disk sampling can generate a set of sampling points randomly and uniformly, it is also often used in image rendering, image processing, and other applications. In our method, we use Poisson distribution to increase the randomness and uniform distribution for the sampled image patches. When generating a new sampling point, we take the sampling point as the center and crop a local image patch with a resolution of 64×64. In our experiments, we have tested the performance of our algorithm with different patch sizes. As the inputs for the 2-channel network, we can set the patch sizes with different resolutions for symmetry detection, including 8×8, 16×16, 32×32, 64×64, and 128×128. Among different patch size settings, we found that a resolution of 64×64 can obtain the best accuracy performance in the following symmetry detection. The Poisson sampling and patches distribution is shown in Fig. 4. For each symmetry axis candidate A_i, we randomly and uniformly pick 100 pairs of patches, which are symmetric with each other in the space domain according to A_i. Note that we also flip the patches in the right hemisphere for the patch matching convenient. Finally, all patch pairs are stored in two sets, which are denoted as $I_{l,i}$ and $I_{r,i}$, respectively. By

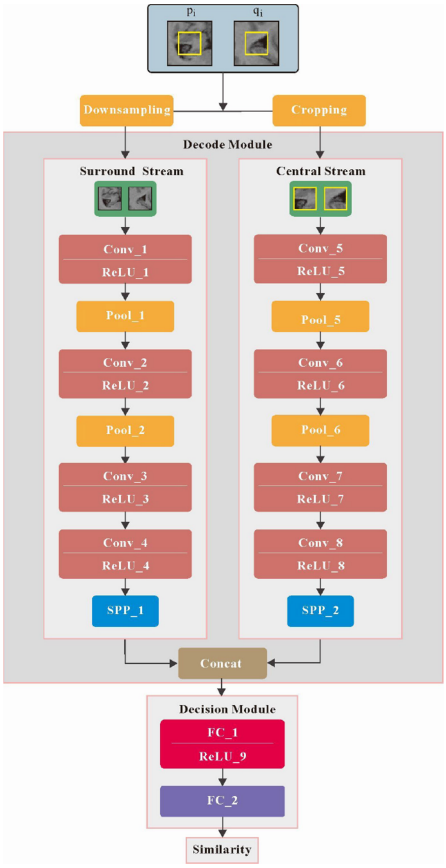

Fig. 5. Architecture of 2-channel CNN.

rotating the initial symmetry axis with a small step from 0° to 180° counterclockwise, we can repeat the above symmetric paths extraction to generate enough image patches data for 2-channel CNN training in the next step.

C. 2-Channel CNN

After brain patches extraction, we need to measure the similarity between each pair of symmetric patches. Similar to Zagoruyko and Komodakis [42], we employ a 2-channel CNN to measure the similarity between two image patches. The idea of 2-channel CNN comes from the Siamese model [43]. The structure of the 2-channel network used to measure patch similarity is as shown in the decode module. Given a pair of patches (p_i and q_i), we first generate two streams of image data for p_i and q_i by downsampling and cropping, as shown in Fig. 5. According to [42], we know that such a multiscale input design is very helpful in improving the network accuracy for patch matching. Specifically, we can see that our network architecture includes a decoded module and a decision module. In the decode module, the branch on the left side of Fig. 5 is the low-resolution channel, which we call it to surround stream. And the branch on the right is the high-resolution channel called the central stream. Obviously, the structure of the two branches is quite similar and including a series of convolution layers, ReLu, and pooling layers. In general, the underlying structure of the two branches can be used as a decoder for the image patch with different resolutions. The

TABLE I
STRUCTURE AND PARAMETERS OF 2-CHANNEL NEURAL NETWORK

2-Channel Network				
	Surround Stream			
Name	Type	Output Dims	Kernel	Stride
Conv1	C	96 × 28 × 28	5 × 5	1
pool1	MP	96 × 14 × 14	2 × 2	2
Conv2	C	96 × 12 × 12	3 × 3	1
Pool2	MP	96 × 6 × 6	2 × 2	2
Conv3	C	192 × 4 × 4	3 × 3	1
Conv4	C	192 × 2 × 2	3 × 3	1
SPP1	SPP	768	-	-
	Central Stream			
Conv5	C	96 × 28 × 28	5 × 5	1
Pool5	MP	96 × 14 × 14	2 × 2	2
Conv6	C	96 × 12 × 12	3 × 3	1
Pool6	MP	96 × 6 × 6	2 × 2	2
Conv7	C	192 × 4 × 4	3 × 3	1
Conv8	C	192 × 2 × 2	3 × 3	1
SPP2	SPP	768	-	-
FC1	FC	768	-	-
FC2	FC	1	-	-

output of the surround stream and central stream is concatenated together as the input to the top layer. The top layer of the decision module is the two fully connected layers. We also use a spatial pyramid network structure to connect the full connection layer and the convolution layer. Finally, we obtain the similarity of two patches from the output of the decision module as a 1-D vector.

As shown in Fig. 5, it is known that a full connection is usually connected behind the convolutional layer for a typical CNN structure. Because the feature number of the entire connection layer is fixed when training the network, the size of the feature map will remain unchanged. As a result, this may require the image patches having a fix resolution as an input. However, we need a more flexible setting because the size of the image patches can be different under different medical imaging environments or other different symmetric patches extraction algorithms. Therefore, we added a spatial pyramid pool (SPP) [44] network between the convolutional layer and the fully connected layer. We can see that after the convolution of the first layer, the pixels of the two images are weighted and mapped. Table I is the detailed parameters of our 2-channel CNN.

D. Learning

We train the network model in a strongly supervision way [42]. First, we trained the objective learning functions based on weighted hinge loss and squared L2 regularization, as the following:

$$\min_{w} \frac{\lambda}{2}\|w\|_2 + \sum_{i=1}^{N} \max\left(0, 1 - y_i o_i^{\text{net}}\right) \tag{3}$$

where w is the weight of our neural network. O_i^{net} is the network output for the ith training sample. And $y_i \in \{-1, 1\}$ is the corresponding label, where we use -1 and 1 to denote a nonmatching and a matching pair, respectively.

In our experiment, various parameters like ASGD with constant learning rate is 1.0. And momentum is 0.9. Weight decay $\lambda = 0.0005$ is used to train the models, where our training is done in mini-batches of size 128. The weights are also initialized randomly, and all models are trained from scratch. To create a better dataset and extend the dataset, we further increase training images by flipping two patches horizontally and vertically and rotating them to 45°, 90°, and 120°, respectively. Overfitting can be ignored in the training step, so we can test the performance of our model after iterating a certain number of times. For our 2-channel networks, we compute descriptors for each pixel in both the two image patches once and then match them with the decision top layer. For implementation detail, we use Titan GPU in Torch, and all convolution routines are taken from Nvidia cuDNN library [45].

E. Scoring and Ranking

After the processing of our 2-channel CNN on the p_i and q_i, we can denote the final 1-D similarity vector $S(A_\theta, i)$ as follows:

$$S(A_\theta, i) = O^{\text{net}}(p_i, q_i) \tag{4}$$

where A_θ represents the symmetry axis candidate on the angle of θ. $O^{\text{net}}(p_i, q_i)$ is the similarity output of the 2-channel CNN for a pair of patches p_i and q_i.

Also, we can further obtain the overall similarity score $G(A_\theta)$ between the two image parts beside the symmetry axis candidate A_θ by a simple summation on patch similarities, which is denoted as follows:

$$G(A_\theta) = \sum_{i=1}^{n} (S(A_\theta, i)) \tag{5}$$

where n is the pair number of patches extracted around the symmetry axis candidate A_θ.

By rotating the initial candidate axis by a small step of 0° to 180° counterclockwise, we can obtain 180 symmetry scores for all axis candidates. Finally, we can obtain the best symmetry axis with a quick sorting algorithm. The optimal axis A_{opt} can be denoted as follows:

$$A_{\text{opt}} = \text{Max}(G(A_0), G(A_1), \ldots, G(A_{180})) \tag{6}$$

where $G(A_i)$ is the symmetry similarity score for a specific symmetry candidate at angle i from 0 to 180. Through a maximum selection, the optimal symmetry axis A_{opt} is determined. For 2-D cases, we can use angle and position errors between our symmetry detection result and the ground-truth to evaluate the performance of our method. In order to accurately define the symmetry axis of the brain MR image, we use the standard polar coordinates to represent the axis of the extracted optimal symmetry axis A_{opt} as follows:

$$r_{\text{opt}} = x_c \cos\theta_{\text{opt}} + y_c \sin\theta_{\text{opt}} \tag{7}$$

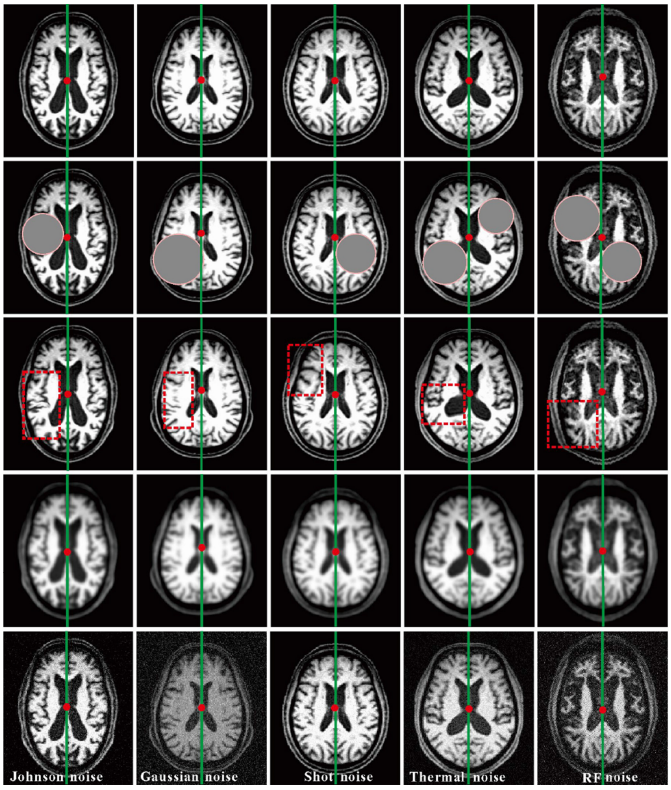

Fig. 6. MSP extracted from the synthetic images with known ground truth (the first row). Artificial tumor, local deformation, Gaussian blur, and different kinds of noises were added to the original images in the second, third, fourth, and fifth rows, respectively.

where (x_c, y_c) is the centroid C_0 of the brain MR image, and θ_{opt} is the angel counterclockwise between the horizontal line and the extracted optimal symmetry axis A_{opt}.

IV. Results

We implemented our method in C on a PC with 4 Intel Xeon CPUs of 3.20 GHz, 32-GB RAM, Nvidia GeForce GTX TITAN Xp GPU and 12-GB video memory. In our experiments, we applied our method in both synthetic and *in vivo* MRI datasets to evaluate its effectiveness in symmetry detection and MSP extraction. Comparisons with three state-of-the-art methods were also conducted to demonstrate its advantages.

A. Evaluation on Synthetic Datasets

As the symmetry axis is very difficult and also time consuming to be manually identified by a clinical doctor, we first generated a synthetic dataset for our brain symmetry detection evaluation. To synthesize a brain MRI with a known symmetry axis ground truth vertically located in the center of the image (as shown in the first row of Fig. 6), we first cropped one half of brain MR image by manually extracting the fissure line from an *in vivo* brain MR image. Then, we created its reflected version by flipping the cropped half image according to the fissure line. Finally, we can successfully synthesize a brain MR image by simply stitching the cropped half image and its flipped version. Obviously, above synthesized brain image has a known symmetry axis ground truth on the fissure line, as the two half images beside it are with an exactly reflectional symmetry relationship. Typical examples are as shown in the first row of Fig. 6, where we can see that the image contents are exactly reflectional symmetry according to the green axis. In our experiments, thousands of perfectly symmetrical brain images were synthesized for our symmetry detection evaluation. For more realistic brain image synthesis, we can also add a certain amount of artificial tumors, deformation, blur, and different kinds of noises (including RF noise, Johnson noise, thermal noise, shot noise, and Gaussian noise) to the synthetic datasets, such as the images shown in Fig. 6. Based on the above-synthesized datasets with known symmetry ground truth, we can evaluate our method quantitatively without any subjective factors from a clinical doctor when drawing the symmetry axis.

We applied our method to perform the symmetry detection for the brain MR images on our synthesized datasets. To observe the accuracy of our method, we presented several representative slices are shown in Fig. 6. The green line is the symmetry axis detected using our method. We can observe that our method can accurately extract the symmetry axis. Note that all symmetry axes are perfectly passing through the centroid of the brains for our synthetic datasets. To further test the tolerance of our method to structural asymmetry, distortion, blur, and noises, we also applied our method on the synthetic datasets with an artificial tumor, distortion, Gaussian blur, and different kinds of noises (including RF noise, Johnson noise, thermal noise, shot noise, and Gaussian noise). The results are as shown in the second to fifth rows of Fig. 6, where we can also observe the stability of our method in successfully identifying the symmetry axes. In our experiment, we used uniform grayscale spheres as artificial tumors. As shown in the second row of Fig. 6, the size and number of artificial tumors in these synthetic spheres are randomly generated. By changing the size and number of artificial tumors, we can test our method's tolerance for structural asymmetry. It can be seen that our method can still accurately extract MSP, even if there have several artificial tumors in the brain, and the size is a quarter of the brain image. To assess the ability to prevent local distortion interference and MR images bias uneven, we also added distractions manually in MR images, such as the locally distorted areas and prejudiced inhomogeneity in the images. Besides, we also add local deformation, Gaussian blur, and different kinds of noises (including RF noise, Johnson noise, thermal noise, shot noise, and Gaussian noise) to the synthesized MR image, as shown in the third to fifth rows of Fig. 6. We can see that our method can successfully identify MSP in MR images with local deformation, Gaussian blur, and different noises. The above results also proved that our 2-channel CNN could robustly detect the ideal symmetry axis, where the artificial tumors, local deformation, Gaussian blur, and different MR noises have minimal impacts on our symmetry detections.

Besides adding artificial tumor, noises, and blur, we also tested the tolerance of our method on the rotations of the brain images. As shown in Fig. 7, we rotated the synthesized MR image counterclockwise by 15°, 30°, 45°, and 120°, respectively. The synthesized database was expanded by five

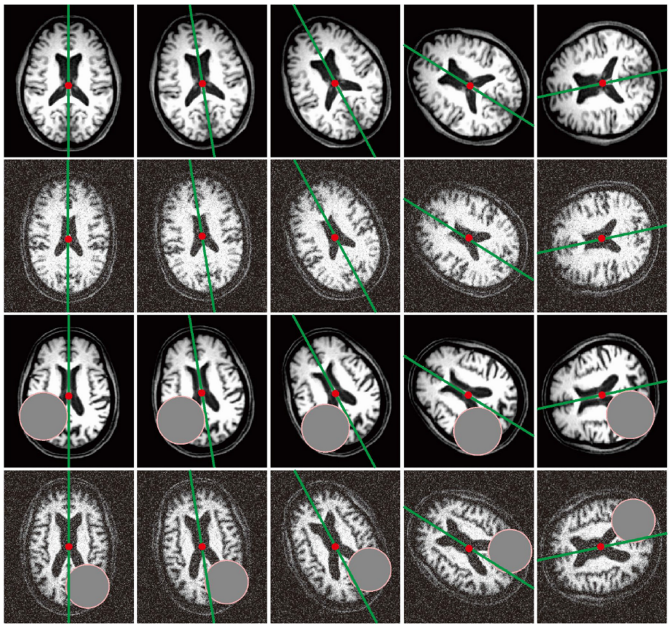

Fig. 7. Symmetry detection in the rotated synthesized examples. The symmetry axes (green lines) are extracted from the synthetic images with known ground truth (the first column) and the brain MR images rotated counterclockwise with an angle of 15°, 30°, 60°, and 120° (in the second, third, fourth, and fifth columns, respectively).

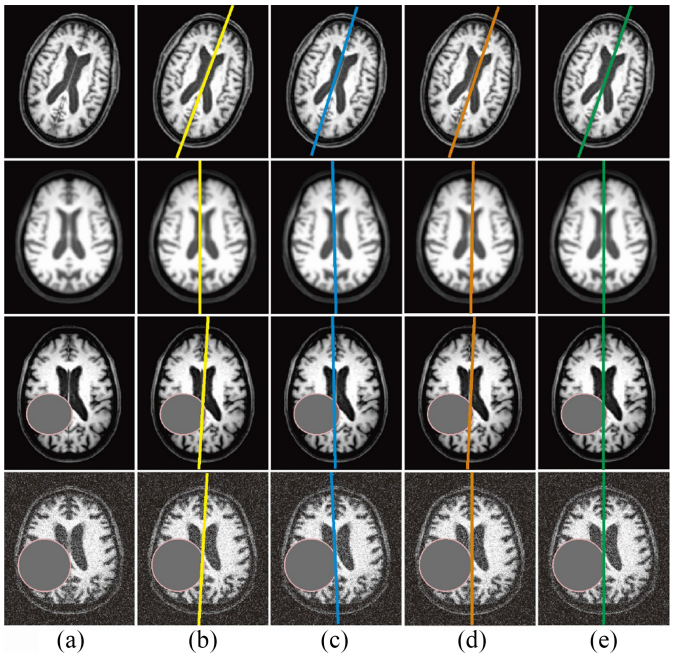

Fig. 8. Visual comparison of different methods in detecting MSP from the synthetic datasets. (a) Input images. The MSP extracted using Wu *et al.* [23], Li *et al.* [17], Ferrari *et al.* [26], and our method are shown in (b)–(e), respectively.

times. In the first row of Fig. 7, we can see that our method can accurately find the MSP in the composite MR images, which are rotated by 15°, 30°, 45°, and 120° counterclockwise. In the second, third, and fourth rows of Fig. 7, we further combined the other three interfering factors, including rotation, noises, and artificial tumor with rotations to test the performance of our method. The results shown in Fig. 7 demonstrated that our method also performed well under the influence of multiple interfering factors, which is also pointing out that our 2-channel CNN has stable performance in the brain symmetry detections.

For a thorough quantitatively comparison, we also implemented three state-of-the-art methods, including Wu *et al.* [23], Li *et al.* [17], and Ferrari *et al.* [26]. To quantitatively verify the tolerance of our method to the rotation, noise, blur, and asymmetry, we applied our method and three other competitors on the synthetic datasets with different degrees of rotations, noises, artificial tumors, and blur, respectively. We randomly selected 65 perfectly symmetrical brain MR images and reconstructed four types of datasets. In our experiments, the four competitors were compared in a total of 1460 synthetic brain MR images with different degrees of rotation, Gaussian noise, Gaussian blur, and artificial tumors. As shown in Fig. 8, the results of Wu *et al.* [23], Li *et al.* [17], Ferrari *et al.* [26], and our method are as shown in (b)–(e) columns of Fig. 8, respectively. As we can see from Fig. 8, Wu *et al.* [23] cannot deal well the data with high blur. The accuracy of MSP extraction is affected when the blur radius (sigma) is more than 12 mm or when the data is suffering from other types of blur. Li *et al.* [17] are not suitable for processing small-scale image data, and the algorithm is greatly affected by the blur and noise. High noise and fuzzy intensity would affect the number of SIFT feature points extracted, resulting in a decrease of algorithm accuracy. Furthermore, there required a prior training template set, and the performance depends on the accuracy of the template. Ferrari *et al.* [26] have a poor performance in detecting MSP on the test cases with large directional rotation, and cannot deal with the occlusion of tumors. Compared with the above traditional approaches, which usually heavily depended on specific feature detection or a prior training template, our deep-learning-based method does not require any feature selection and detection. Moreover, the experiments also demonstrated that our method generally outperformed the three state-of-the-art methods in the brain symmetry detection. So our 2-channel CNN is not only superior to existing single-channel CNN with a two-scale brain representation but also superior to the state-of-the-art of feature-based methods.

In addition to visual comparison, we also calculated the polar angle error (in degrees) and radius error (in millimeters) between the detected MSP (r_d, θ_d) and the ground truth value axis of symmetry (r_g, θ_g) for quantitative comparison with our method and the other competitors. To evaluate the tolerance of rotation, we first rotated the MR brain images counterclockwise by 20°, 40°, 60°, 80°, 100°, and 120°, respectively. Second, we produced different degrees of the noise of −5, −10, −15, −20, −25, and −30 db on the MR brain images to evaluate the noise tolerance. Third, we also created a Gaussian blur with a blur radius of 2, 4, 6, 8, 10, and 12 mm on the MR brain images to evaluate the tolerance of blur. Besides, we further generated artificial tumors with a radius of 20, 40, 60, 80, 90, and 100 mm on the MR brain images to evaluate the tolerance of asymmetry for different methods. Finally, we plotted the mean polar error and radius

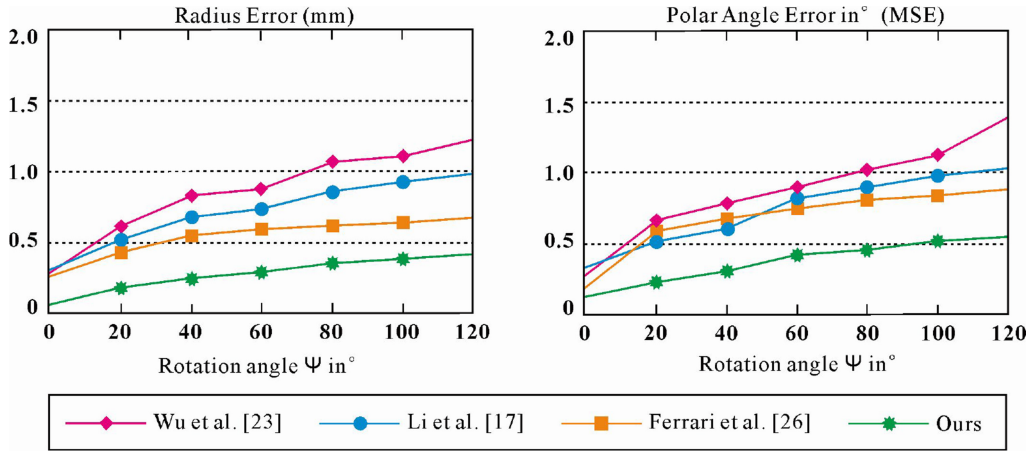

Fig. 9. Comparison of different methods in tolerance to rotation.

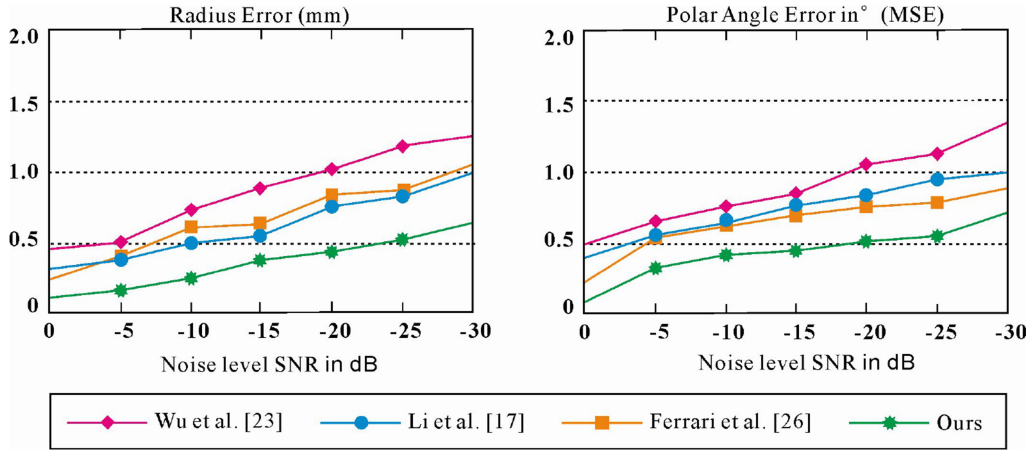

Fig. 10. Comparison of different methods in tolerance to noise.

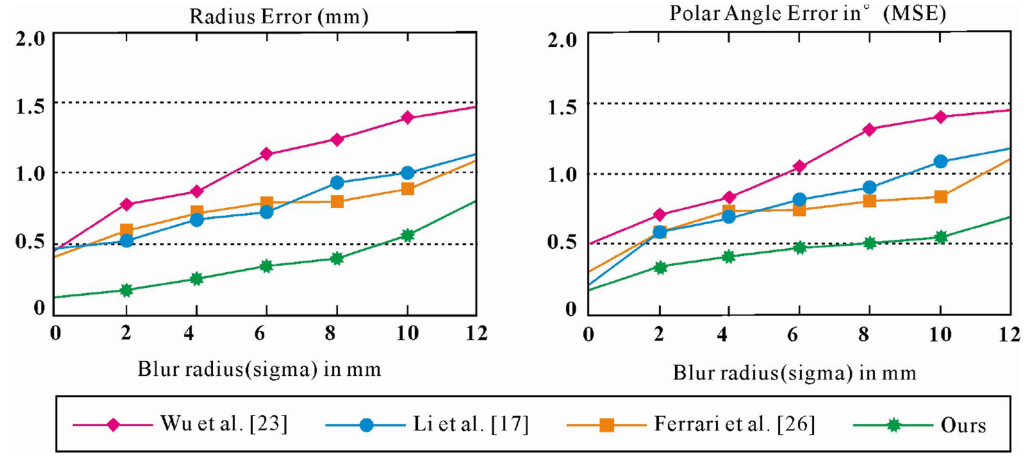

Fig. 11. Comparison of different methods in tolerance to blur.

error between our method and the other three competitors on the synthetic datasets with different degrees of rotation, noise, blur, and asymmetry occlusion, as shown in Figs. 9–12. From the results, we can know that our deep-learning-based method also generally outperformed the other three competitors in the accuracy of both angular and radius in polar coordinates. Furthermore, it can be observed that our method has a much more significant accuracy improvement if there have heavier degrees in rotation (Fig. 9), noise (Fig. 10), blur (Fig. 11), or asymmetry (Fig. 12). This also points out the importance of using a 2-channel CNN framework to detect the symmetry axis.

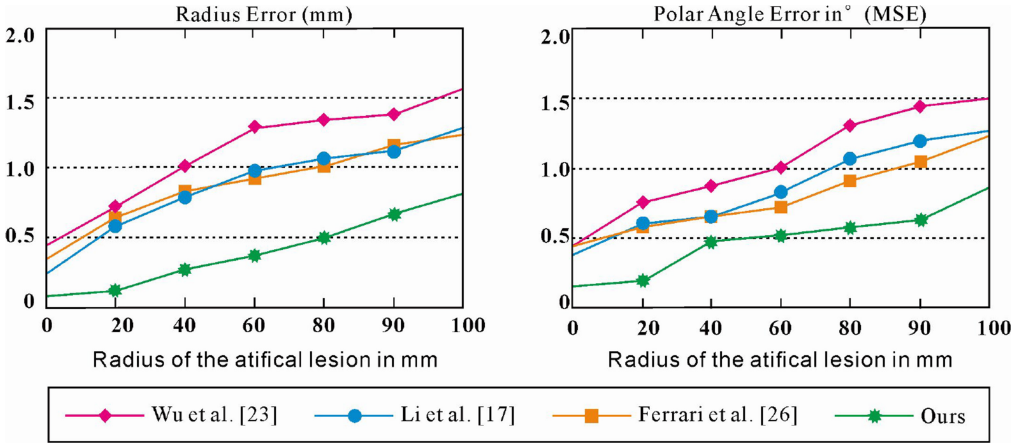

Fig. 12. Comparison of different methods in tolerance to occlusion of the artificial tumors.

TABLE II
In Vivo DATASETS COLLECTED FOR EVALUATION

Datasets	Pathology	# of slices
1	Normal	708
2	Glioma	426
3	Meningioma	643
4	Pituitary Tumor	930

TABLE III
ACCURACY STATISTICS OF DIFFERENT METHODS FOR THE *In Vivo* DATASETS

	Polar Angle Error (°)										
	Wu et al. [23]			**Li** et al. [17]			**Ferrari** et al. [26]			**Our method**	
Datasets	Mean	SD	P-value	Mean	SD	P-value	Mean	SD	P-value	Mean	SD
1	0.686	0.370	0.0036	0.411	0.320	0.0093	0.431	0.289	0.0124	0.173	0.256
2	0.943	0.363	0.0051	0.813	0.335	0.0095	0.691	0.334	0.0128	0.420	0.293
3	0.974	0.358	0.0046	0.768	0.327	0.0089	0.651	0.356	0.0126	0.417	0.287
4	0.969	0.371	0.0054	0.802	0.380	0.0087	0.643	0.337	0.0116	0.415	0.270
	Radius Error (mm)										
	Wu et al. [23]			**Li** et al. [17]			**Ferrari** et al. [26]			**Our method**	
Datasets	Mean	SD	P-value	Mean	SD	P-value	Mean	SD	P-value	Mean	SD
1	0.660	0.392	0.0039	0.443	0.313	0.0099	0.456	0.273	0.0116	0.231	0.247
2	0.957	0.361	0.0048	0.836	0.339	0.0092	0.702	0.331	0.0117	0.439	0.261
3	0.981	0.358	0.0045	0.857	0.354	0.0092	0.698	0.336	0.0115	0.440	0.282
4	0.955	0.370	0.0046	0.829	0.332	0.0095	0.693	0.341	0.0120	0.438	0.273

B. Evaluation on the In Vivo Datasets

On the other hand, we also evaluated our proposed method on the *in vivo* datasets, including both normal and patient cases. As shown in Table II, we collected a total of 3064 *in vivo* MR images from both normal and patient brains based on an open-access brain MRI dataset [46]. More specifically, our *in vivo* datasets include 708 images from normal subjects, 426 images from patients with meningiomas, 643 images from patients with gliomas, and 930 images from patients with pituitary tumors. Similar to the real clinical conditions, our datasets are diverse enough for the brain symmetry detection evaluations. Based on the above *in vivo* datasets, we still applied our method and the other three state-of-the-art methods to perform symmetry detection for real brain images. The results for the four different symmetry detection methods are as shown in Fig. 13. Since there is no existing ground truth of MSP for the collected datasets, we invited a clinical expert to draw a line (red) to be the symmetry axis manually. Typical examples of the manual results are as shown in Fig. 13(a), which can be treated as the ground truth for the *in vivo* datasets. To make the comparison results more clearly, we have over imposed the MSP results obtained by different methods with the one drawn manually by a clinical expert. Therefore, we can compare the results of four automatic methods [Fig. 13(b)–(e)] with the manual results [Fig. 13(a)]. From the visual comparison, we can obviously observe that none of the three competitors can achieve a stable symmetry detection because they heavily relied on the gray level, skull shape, or internal edges to determine the symmetry axes, which is sensitive to local image deformation, noise, or asymmetry. By using a more stable 2-channel CNN framework, our method generally outperformed the other methods. Thanks to the ability of our method in handling images with multiresolution or complex structures, we can clearly see that our results are more close to the clinical expert's results, especially, when the images have imaging noise, local deformations, or brain tumors. In addition, we also calculated the mean error between the clinical expert and each competitor, as shown in Table III. To evaluate if our improvement is statistically significant, we also calculated a P-value using mixed model analysis to compare our method with each state-of-the-art method. As shown in Table III, compared with other methods, our method has significant improvement in terms of accuracy of both polar angle and radius at the 5% level (P-value is less than 0.05).

To test the efficiency, we further estimated the average running time of our method and the other three methods. In our experiments, we selected 300 brain MR images (256×256) from the *in vivo* datasets. To further evaluate the efficiency of different methods in handling brain images with different resolutions, we also resized the 300 cases into 128×128 and 512×512 by down sampling and up sampling. Then, we applied our method and the other three competitors repeatedly on the 300 cases with three different resolutions and collected

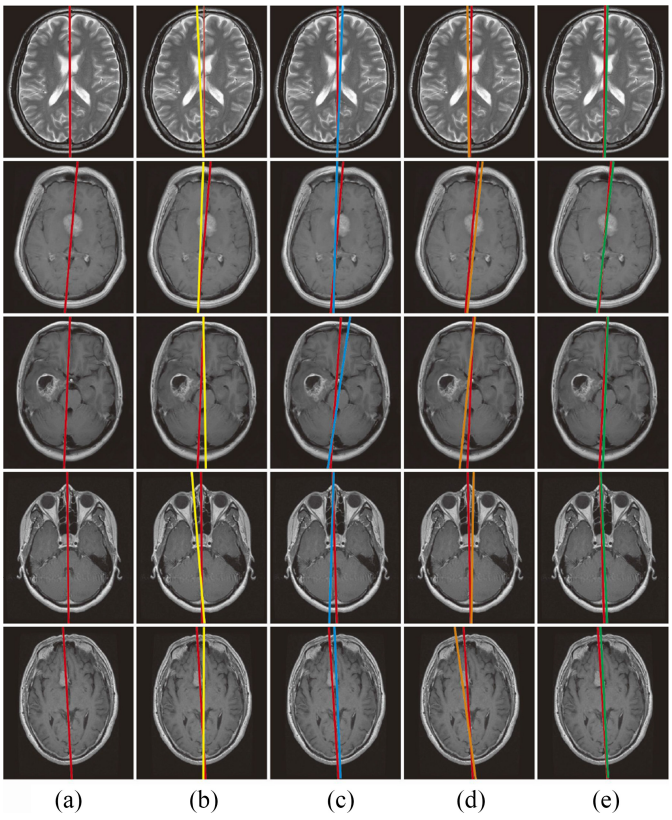

Fig. 13. Visual comparison of different methods *in vivo* datasets. (a) MSP (red) drawn manually by a clinical expert. MSP results of Wu *et al.* [23] (yellow), Li *et al.* [17] (blue), Ferrari *et al.* [26] (orange), and our method (green) over imposed on the results of clinical expert are as shown in (b)–(e), respectively.

TABLE IV
AVERAGE RUNNING TIME COMPARISON OF DIFFERENT METHODS FOR THE *In Vivo* DATASETS

Image size	Average Running Time (in second)			
	Wu et al. [23]	**Li** et al. [17]	**Ferrari** et al. [26]	**Our method**
128 X 128	2.364	2.588	4.159	1.959
256 X 256	2.657	3.034	4.950	2.103
512 X 512	2.783	4.316	5.385	2.240

TABLE V
AVERAGE RUNNING TIME FOR EACH STEPS IN OUR METHOD

Image size	Average Running Time (in second)				
	HED CNN	Poisson sampling	2-Channel CNN	Scoring & Ranking	Total
128 X 128	0.576	0.08	1.273	0.03	1.959
256 X 256	0.608	0.08	1.385	0.03	2.103
512 X 512	0.631	0.08	1.499	0.03	2.240

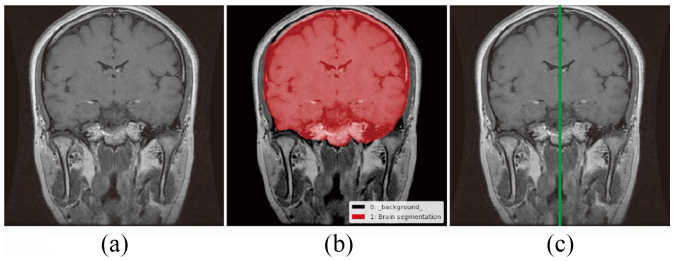

Fig. 14. Brain MRI with a part of neck and artifacts. (a) Brain MRI. (b) Segmentation. (c) Result.

the average running time. Since the training of the parameters for our 2-channel, CNN can be done offline and only be required done a single time, so it is unnecessary to include the training time for our symmetry detection. The statistics of running time for different methods on our selected dataset is as shown in Table IV. In addition, we also collected the average running time for each step in our method to evaluate the computational complexity of our method, as shown in Table V. From the statistical results, we can clearly observe that our method also outperforms the other three methods because our method does not require any specific image feature detection and selection.

C. Discussions and Limitations

Through the comparison experiments for both synthetic and *in vivo* datasets, we can see that our method has excellent tolerance to the rotation, blur, artificial tumor asymmetry, and different types of noise in MR images, including RF noise, Johnson noise, thermal noise, and shot noise. Compared with the traditional local feature descriptors, the feature maps extracted by our 2-channel CNN contain much more detailed semantics and structural information. Unlike the single-channel CNN, which may only consider the input image under one static resolution, our 2-channel CNN can learn much more multiscale detailed feature maps in the texture semantic level [47]. As a result, the feature maps in the texture semantic level usually can better explain the subtle changes between brain image patches. So the results of our experiments benefit from our unique 2-channel CNN design, with an excellent tolerance ability to local image deformation, noise, or asymmetric interference. Moreover, our 2-channel CNN-based symmetry detection method can be further extended to other image processing applications.

Currently, our brain MR slices are collected with the horizontal imaging planes, which is perpendicular to the central axis of our human body. So we can always see the clear (whole) images in our results. If the images contain a part of the neck or artifacts of the cerebral cortex, we need a segmentation preprocessing to crop the brain and remove the neck or other artifacts. As our aim is only to extract the ideal MSP from the brain images, the neck and other artifacts should not be taken into account. A typical example is as shown in Fig. 14, the segmentation result in Fig. 14(b) is obtained using a state-of-the-art method [48]. We can see that our method can also handle well that case with a segmentation preprocessing.

Although our method is a novel framework for brain symmetry detection, our proposed method is still based on a combination of several existing techniques, including Poisson disk sampling, HED CNN, and 2-channel CNN. Fortunately, our technique combination has been well validated. A Poisson disk sampling is an excellent sampling technique widely used in image rendering, image processing, and other applications, so we can obtain a set of sampling points randomly and uniformly distributed in the brain images. The CNN-based

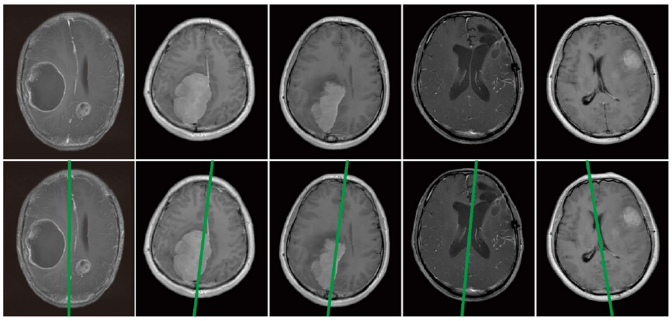

Fig. 15. Failure cases. Our method has limitation when the MSP is a curve.

techniques also have been well verified and widely applied in the other applications of image matching and image registration, so our method can obtain a stable performance in symmetry detection based on the above combination.

On the other hand, our method still also has limitations. Similar to most previous methods for detecting MSP of the brain, our method also assumes that the ideal symmetry axis in the brain image is a straight line. It is proved that the true anatomical structure of the human brain may contain a fissure line exhibiting nonlinearity due to tumors or injuries. Therefore, the assumption that the brain MSP is a straight line has limitations. Fig. 15 shows several failure examples, where we can clearly see that the axis of the brain is a curve. Based on the straight-line assumption, our experiments also demonstrated that our method cannot handle well when the MSP is a curve. However, because we may only require to identify a reference symmetry axis in a brain MR image under several situations, so our 2-channel CNN-based brain symmetry detection method still provides an excellent tool for clinical applications.

V. Conclusion

In this article, we presented a 2-channel CNN-based symmetry detection method for 2-D MR images. Our contribution is that we proposed the first deep-learning framework to extract the fissure line by learning a symmetry representation for the human brain. Unlike the conventional feature-based symmetry detection methods, our method does not require any feature detection and specific matching operations. Specifically, we used a Poisson sampling to randomly and uniformly extract a number of pairs of brain image patches, which may have various resolutions to satisfy SPP structures in the CNN framework. Our 2-channel CNN with both high- and low-resolution channels is then used to compare brain patches based on central and surround structures. Finally, the optimal symmetry axis is determined based on a scoring and ranking scheme. Our method is evaluated with both artificial and *in vivo* brain datasets. Convincing experimental results verified the effectiveness of our method in achieving high accuracy of symmetry detection. Comparisons with the state-of-the-art methods also conducted to demonstrate that our method outperformed the existing feature-based symmetry detection methods in both accuracy and efficiency.

References

[1] S. H. Davarpanah and A. W.-C. Liew, "Spatial possibilistic fuzzy C-mean segmentation algorithm integrated with brain mid-sagittal surface information," *Int. J. Fuzzy Syst.*, vol. 19, no. 2, pp. 591–605, 2017.

[2] H. Gray and C. M. Goss, "Anatomy of the human body," *Amer. J. Phys. Med. Rehabil.*, vol. 53, no. 6, p. 293, 1974.

[3] Y. Sun, Y. Chen, S. L. Collinson, A. Bezerianos, and K. Sim, "Reduced hemispheric asymmetry of brain anatomical networks is linked to schizophrenia: A connectome study," *Cerebral Cortex*, vol. 27, no. 1, pp. 602–615, 2017.

[4] G. E. Bruder, J. W. Stewart, and P. J. McGrath, "Right brain, left brain in depressive disorders: Clinical and theoretical implications of behavioral, electrophysiological and neuroimaging findings," *Neurosci. Biobehav. Rev.*, vol. 78, pp. 178–191, Jul. 2017.

[5] L. Gao, P. Smielewski, M. Czosnyka, and A. Ercole, "Early asymmetric cardio-cerebral causality and outcome after severe traumatic brain injury," *J. Neurotrauma*, vol. 34, no. 19, pp. 2743–2752, 2017.

[6] B. P¨ottker *et al.*, "Traumatic brain injury causes long-term behavioral changes related to region-specific increases of cerebral blood flow," *Brain Struct. Funct.*, vol. 222, no. 9, pp. 4005–4021, 2017.

[7] C.-P. Yu, G. C. S. Ruppert, D. T. D. Nguyen, A. X. Falcão, and Y. Liu, "Statistical asymmetry-based brain tumor segmentation from 3D MR images," in *Proc. Int. Conf. Bio Inspired Syst. Signal Process.*, 2012, pp. 527–533.

[8] L. Minkova, A. Habich, J. Peter, C. P. Kaller, S. B. Eickhoff, and S. Kl¨ppel, "Gray matter asymmetries in aging and neurodegeneration: A review and meta-analysis," *Human Brain Mapping*, vol. 38, no. 12, pp. 5890–5904, 2017.

[9] J. L. Lancaster, T. G. Glass, B. R. Lankipalli, H. Downs, H. Mayberg, and P. T. Fox, "A modality-independent approach to spatial normalization of tomographic images of the human brain," *Human Brain Mapping*, vol. 3, no. 3, pp. 209–223, 1995.

[10] S. X. Liu, "Symmetry and asymmetry analysis and its implications to computer-aided diagnosis: A review of the literature," *J. Biomed. Informat.*, vol. 42, no. 6, pp. 1056–1064, 2009.

[11] J. Bernal *et al.*, "Deep convolutional neural networks for brain image analysis on magnetic resonance imaging: A review," *Artif. Intell. Med.*, vol. 95, pp. 64–81, Apr. 2019.

[12] Y. Wei *et al.*, "Cross-modal retrieval with CNN visual features: A new baseline," *IEEE Trans. Cybern.*, vol. 47, no. 2, pp. 449–460, Feb. 2017.

[13] J. Han, H. Chen, N. Liu, C. Yan, and X. Li, "CNNs-based RGB-D saliency detection via cross-view transfer and multiview fusion," *IEEE Trans. Cybern.*, vol. 48, no. 11, pp. 3171–3183, Nov. 2018.

[14] A. Dobai, Z. Markella, T. Vízkelety, C. Fouquet, A. Rosta, and J. Barabás, "Landmark-based midsagittal plane analysis in patients with facial symmetry and asymmetry based on CBCT analysis tomography," *J. Orofacial Orthopedics/Fortschritte der Kieferorthop´adie*, vol. 79, no. 6, pp. 371–379, 2018.

[15] A. Jajoo *et al.*, "Calculating the midsagittal plane for symmetrical bilateral shapes: Applications to clinical facial surgical planning," *CoRR*, vol. abs/1803.05853, pp. 1–16, 2018.

[16] W. Gao, X. Chen, Y. Fu, and M. Zhu, "Automatic extraction of the centerline of corpus callosum from segmented mid-sagittal MR images," *Comput. Math. Methods Med.*, vol. 2018, Jul. 2018, Art. no. 4014213.

[17] W. Li, H. Pan, X. Xie, Z. Zhang, and Q. Han, "Simple and robust ideal mid-sagittal line (iML) extraction method for brain CT images," in *Proc. IEEE 16th Int. Conf. Bioinformat. Bioeng. (BIBE)*, Taichung, Taiwan, 2016, pp. 266–273.

[18] Y. Zhang and Q. Hu, "A PCA-based approach to the representation and recognition of MR brain midsagittal plane images," in *Proc. 30th Annu. Int. Conf. IEEE Eng. Med. Biol. Soc.*, Vancouver, BC, Canada, 2008, pp. 3916–3919.

[19] S. X. Liu, J. Kender, C. Imielinska, and A. Laine, "Employing symmetry features for automatic misalignment correction in neuroimages," *J. Neuroimag.*, vol. 21, no. 2, pp. e15–e33, 2011.

[20] N. Ray, R. Greiner, and A. Murtha, "Using symmetry to detect abnormalities in brain MRI," *Comput. Soc. India Commun.*, vol. 31, no. 19, pp. 7–10, 2008.

[21] Q. Hu and W. L. Nowinski, "A rapid algorithm for robust and automatic extraction of the midsagittal plane of the human cerebrum from neuroimages based on local symmetry and outlier removal," *NeuroImage*, vol. 20, no. 4, pp. 2153–2165, 2003.

[22] H. Cornelius and G. Loy, "Detecting rotational symmetry under affine projection," in *Proc. 18th Int. Conf. Pattern Recognit. (ICPR)*, vol. 2, 2006, pp. 292–295.

[23] H. Wu, D. Wang, L. Shi, Z. Wen, and Z. Ming, "Fast and robust symmetry detection for brain images based on parallel scale-invariant feature transform matching and voting," *Int. J. Imag. Syst. Technol.*, vol. 23, no. 4, pp. 314–326, 2013.
[24] C.-C. Liao, F. Xiao, J.-M. Wong, and I.-J. Chiang, "Automatic recognition of midline shift on brain CT images," *Comput. Biol. Med.*, vol. 40, no. 3, pp. 331–339, 2010.
[25] F. Xiao, I.-J. Chiang, J.-M. Wong, Y.-H. Tsai, K.-C. Huang, and C.-C. Liao, "Automatic measurement of midline shift on deformed brains using multiresolution binary level set method and Hough transform," *Comput. Biol. Med.*, vol. 41, no. 9, pp. 756–762, 2011.
[26] R. J. Ferrari, C. H. V. Pinto, and C. A. F. Moreira, "Detection of the midsagittal plane in MR images using a sheetness measure from eigenanalysis of local 3D phase congruency responses," in *Proc. IEEE Int. Conf. Image Process. (ICIP)*, Phoenix, AZ, USA, 2016, pp. 2335–2339.
[27] Y. Liu and B. M. Dawant, "Automatic localization of the anterior commissure, posterior commissure, and midsagittal plane in MRI scans using regression forests," *IEEE J. Biomed. Health Inform.*, vol. 19, no. 4, pp. 1362–1374, Jul. 2015.
[28] H. Yan, J. Lu, and X. Zhou, "Prototype-based discriminative feature learning for kinship verification," *IEEE Trans. Cybern.*, vol. 45, no. 11, pp. 2535–2545, Nov. 2015.
[29] A. Majumder, L. Behera, and V. K. Subramanian, "Automatic facial expression recognition system using deep network-based data fusion," *IEEE Trans. Cybern.*, vol. 48, no. 1, pp. 103–114, Jan. 2018.
[30] H. Wang, J. Peng, and S. Yue, "A directionally selective small target motion detecting visual neural network in cluttered backgrounds," *IEEE Trans. Cybern.*, to be published.
[31] C. Cao, Y. Zhang, C. Zhang, and H. Lu, "Body joint guided 3-D deep convolutional descriptors for action recognition," *IEEE Trans. Cybern.*, vol. 48, no. 3, pp. 1095–1108, Mar. 2018.
[32] B. Pourbabaee, M. J. Roshtkhari, and K. Khorasani, "Deep convolutional neural networks and learning ECG features for screening paroxysmal atrial fibrillation patients," *IEEE Trans. Syst., Man, Cybern., Syst.*, vol. 48, no. 12, pp. 2095–2104, Dec. 2018.
[33] P. Moeskops, M. Veta, M. W. Lafarge, K. A. Eppenhof, and J. P. Pluim, "Adversarial training and dilated convolutions for brain MRI segmentation," in *Deep Learning in Medical Image Analysis and Multimodal Learning for Clinical Decision Support*. Cham, Switzerland: Springer, 2017, pp. 56–64.
[34] B. Sheng *et al.*, "Retinal vessel segmentation using minimum spanning superpixel tree detector," *IEEE Trans. Cybern.*, vol. 49, no. 7, pp. 2707–2719, Jul. 2019.
[35] S. Korolev, A. Safiullin, M. Belyaev, and Y. Dodonova, "Residual and plain convolutional neural networks for 3D brain MRI classification," in *Proc. IEEE 14th Int. Symp. Biomed. Imag. (ISBI)*, Melbourne, VIC, Australia, 2017, pp. 835–838.
[36] S. S. M. Salehi, D. Erdogmus, and A. Gholipour, "Auto-context convolutional neural network (Auto-Net) for brain extraction in magnetic resonance imaging," *IEEE Trans. Med. Imag.*, vol. 36, no. 11, pp. 2319–2330, Nov. 2017.
[37] F. Liao, X. Chen, X. Hu, and S. Song, "Estimation of the volume of the left ventricle from MRI images using deep neural networks," *IEEE Trans. Cybern.*, vol. 49, no. 2, pp. 495–504, Feb. 2019.
[38] K. Kamnitsas *et al.*, "Efficient multi-scale 3D CNN with fully connected CRF for accurate brain lesion segmentation," *Med. Image Anal.*, vol. 36, pp. 61–78, Feb. 2017.
[39] M. Shakeri *et al.*, "Sub-cortical brain structure segmentation using F-CNN'S," in *Proc. IEEE 13th Int. Symp. Biomed. Imag. (ISBI)*, Prague, Czech Republic, 2016, pp. 269–272.
[40] S. Xie and Z. Tu, "Holistically-nested edge detection," in *Proc. IEEE Int. Conf. Comput. Vis.*, 2015, pp. 1395–1403.
[41] R. Bridson, "Fast Poisson disk sampling in arbitrary dimensions," in *Proc. SIGGRAPH Sketches*, San Diego, CA, USA, 2007, p. 22.
[42] S. Zagoruyko and N. Komodakis, "Learning to compare image patches via convolutional neural networks," in *Proc. IEEE Conf. Comput. Vis. Pattern Recognit.*, 2015, pp. 4353–4361.
[43] J. Bromley, I. Guyon, Y. LeCun, E. S$\acute{}$ackinger, and R. Shah, "Signature verification using 'siamese' time delay neural network," in *Proc. Adv. Neural Inf. Process. Syst.*, 1994, pp. 737–744.
[44] K. He, X. Zhang, S. Ren, and J. Sun, "Spatial pyramid pooling in deep convolutional networks for visual recognition," *IEEE Trans. Pattern Anal. Mach. Intell.*, vol. 37, no. 9, pp. 1904–1916, Sep. 2015.
[45] S. Chetlur *et al.*, "cuDNN: Efficient primitives for deep learning," *CoRR*, vol. abs/1410.0759, pp. 1–9, 2014.
[46] C. Jun. (2017). *Brain Tumor Dataset*. [Online]. Available: https://figshare.com/articles/brain_tumor_dataset/1512427/5
[47] R. Geirhos, P. Rubisch, C. Michaelis, M. Bethge, F. A. Wichmann, and W. Brendel, "Imagenet-trained CNNs are biased towards texture; increasing shape bias improves accuracy and robustness," *CoRR*, vol. abs/1811.12231, pp. 1–22, 2018.
[48] X. Bai, Y. Zhang, H. Liu, and Z. Chen, "Similarity measure-based possibilistic FCM with label information for brain MRI segmentation," *IEEE Trans. Cybern.*, vol. 49, no. 7, pp. 2618–2630, Jul. 2019.

Huisi Wu received the B.E. and M.E. degrees in computer science from Xi'an Jiaotong University, Xi'an, China, in 2004 and 2007, respectively, and the Ph.D. degree in computer science from the Chinese University of Hong Kong, Hong Kong, in 2011.

He is currently an Associate Professor with the College of Computer Science and Software Engineering, Shenzhen University, Shenzhen, China. His research interests include computer graphics, image processing, and medical imaging.

Xiujuan Chen received the B.S. degree in information management and information systems from the Kunming University of Science and Technology, Kunming, China, in 2017. She is currently pursuing the master's degree with Shenzhen University, Shenzhen, China.

Her research interests include computer vision, medical imaging, and pattern recognition.

Ping Li (M'14) received the Ph.D. degree in computer science and engineering from the Chinese University of Hong Kong, Hong Kong.

He is currently a Research Assistant Professor with Hong Kong Polytechnic University, Hong Kong. He has one image/video processing national invention patent, and has excellent research project reported worldwide by *ACM TechNews*. His current research interests include image/video stylization, artistic rendering and synthesis, and creative media.

Zhenkun Wen received the M.Sc. degree in science and technology from Tsinghua University, Beijing, China, in 1999.

He is currently a Professor of computing and software and the Director of the Science and Technology Department, Shenzhen University, Shenzhen, China. His research interests include video tampering detection and location, video information security, and medical imaging.